https://doi.org/10.5194/amt-2022-317
Preprint. Discussion started: 23 January 2023

Atmospheric Measurement Techniques Discussions
Open Access

The S/Z Relationship of Rimed Snow Particles

Shelby Fuller [1], Sam Marlow [1], Samuel Haimov [1], Matthew Burkhart [1], Kevin Shaffer [1], Austin Morgan [1], and Jefferson R. Snider [1,2]

[1] Department of Atmospheric Science, University of Wyoming, Laramie, WY

[2] Corresponding Author, jsnider@uwyo.edu

https://doi.org/10.5194/amt-2022-317
Preprint. Discussion started: 23 January 2023

Atmospheric Measurement Techniques Discussions

Abstract

Values of liquid-equivalent snowfall rate (S) at a ground site, and microwave reflectivity (Z) retrieved above the ground site using an airborne W-band radar, were acquired during overflights. Temperature at the ground site was between -6 and -15 ^{o}C. At flight level, within clouds containing ice and supercooled liquid water, the temperature was approximately 7 ^{o}C colder. Additionally, airborne measurements of snow particle imagery were acquired. The images demonstrate that most of the snow particles were rimed. The S/Z pairs are generally consistent with a published S/Z relationship. The latter was developed with airborne measurements of snow particle imagery, which were used to calculate S, and coincident airborne W-band radar measurements, for Z. Both the previous work and this contribution indicate that most S/Z relationships developed for W-band radars underestimate S in situations with rimed snow particles and with Z < 1 mm^6 m^{-3}.

https://doi.org/10.5194/amt-2022-317
Preprint. Discussion started: 23 January 2023

Atmospheric Measurement Techniques Discussions

1 - Introduction

Improvement of methods used to measure snowfall and rainfall are an ongoing focus of meteorological research. The various methods are ground-based instruments that evaluate the mass of precipitation that falls into or onto a collector (precipitation gauges) (Brock and Richardson 2001), ground-based radars (Wilson and Brandes 1979), and airborne and space-borne radars (Matrosov 2007; Kulie and Bennartz 2009; Geerts et al. 2010; Skofronick-Jackson et al. 2017). An objective of these approaches, whether used to make observations independent of other methods (e.g., Kulie and Bennartz 2009), or as a component of multiple observations (e.g., Cocks et al. 2016), is estimation of precipitation rate and accumulation.

Many studies have investigated using radar for evaluating rainfall (for a review see Wilson and Brandes 1979). There are two approaches. The first is research, both observational and computational, that probes the relationship between rainfall rate (R) and radar-measured values of backscattered microwave power. The latter is commonly reported as an equivalent radar reflectivity factor (Z_e). The second is operational in the sense that precipitation gauges are used to calibrate measurements acquired using weather surveillance radars. Complications associated with converting Z_e to R, or converting a radar reflectivity factor[1] (Z) to R, can be grouped in four categories: 1) Inaccuracy in quantification of Z, 2) variation of the R/Z relationship stemming from precipitation processes (e.g., evaporation, coalescence, and break up), 3) difference between the volume of a radar range gate versus the much smaller volume of atmosphere sampled as precipitation falls to a gauge, and 4) vertical displacement between a radar range gate and a calibrating gauge, especially at far ranges.

[1] Radars are calibrated to report Z_e (Smith 1984). Herein, radar reflectivities are reported as $Z = Z_e$ and as $dBZ = 10\log_{10}(Z_e)$.

https://doi.org/10.5194/amt-2022-317
Preprint. Discussion started: 23 January 2023

Atmospheric Measurement Techniques Discussions

For situations with snowfall, methods employing either gauge or radar are associated with complications beyond that incurred in rainfall (Matrosov 2007; Martinaitis et al. 2015; Cocks et al. 2016). Problems associated with gauge measurements are wind-induced snow particle undercatch, gauge capping, delayed registration, and blowing snow aliasing as snowfall. Moreover, in a situation with snow particles most abundant within a radar range gate, compared to rain drops, and where a measurement of Z is used to infer R via a R/Z relationship, the resultant precipitation rate will likely be inaccurate. This is because hydrometeor shape, density, and dielectric properties are all variable for snow particles while relatively invariant for rain drops. Additionally, a snow particle's terminal fall speed varies with size (as is the case for drops) and with particle shape and particle density. Going forward, we refer to the latter two properties as shape and density.

In calculations of Z and liquid-equivalent snowfall rate (S), obtained for the operating wavelength of the nadir-looking radar carried on the CloudSat satellite (wavelength λ = 3.2 mm), density is an important parameter. In these calculations, density is commonly estimated using empirical data (Matrosov 2007; Kulie and Bennartz 2009; Pokharel and Vali 2011, [PV11]). For graupel, a snow particle that grows via collection of supercooled cloud droplets in a process commonly referred to as riming, paired observations of particle mass and particle size have been used to estimate density. There is considerable uncertainty in this approach. Based on data collected at two northwestern US surface sites (Zikmunda and Vali 1972; Locatelli and Hobbs 1974), density values differ by at least a factor of two at particle sizes smaller than 2000 μm (PV11; their Figure 4). Given that the density of rime ice varies with droplet impact speed, droplet size, and temperature (Macklin 1962), it is not surprising that the density-versus-size relationships analyzed by PV11 are so varied.

https://doi.org/10.5194/amt-2022-317
Preprint. Discussion started: 23 January 2023

Our work analyzes values of *Z* acquired using an airborne radar that operates in the W-band (λ = 3.2 mm). In satellite, airborne, and ground installations, W-band radars are used to retrieve *Z* and the latter is converted to S using a S/Z relationship. W-band S/Z relationships are developed in Matrosov (2007), Kulie and Bennartz (2009), Geerts et al. (2010), and PV11. This contribution attempts to refine estimates of S based on W-band radar observations and particularly where the dominant particle type is either rimed crystals or graupel.

The following introductory paragraphs overview W-band S/Z relationships being applied in instances of snowfall where mass is acquired by vapor deposition (crystal), by collection of crystals (aggregate), and by riming (rimed crystal and graupel). Henceforth, the latter two snow particle types are collectively referred to as rimed snow particles.

In a computational study, Matrosov (2007) reported an upper-limit and a lower-limit S/Z relationship for both the crystal and aggregate particle types. Both were modeled as oblate spheroids. The upper-limit and a lower-limit relationships are $S = 0.11 \cdot Z^{1.25}$ and $S = 0.041 \cdot Z^{1.25}$. At any value of *Z* these differ by a factor of 2.7. This variance stems from changes in density, shape, and fall speed as these changes are propagated through cloud-microphysical and microwave-scattering computations. Similar analyses were conducted by Kulie and Bennartz (2009). Both Matrosov (2007) and Kulie and Bennartz (2009) state that the S/Z relationships they recommend should be applied cautiously in settings where rimed snow particles dominate.

In a hybrid approach (computational and an analysis of airborne observations), PV11 concluded that most of the snow particles they imaged were rimed snow particles. Their calculations of S and *Z*, conducted using two density-size relationships (indicated with ρ_1 and ρ_3), were also presented. They compared their calculated reflectivities to measurements of Z from a W-band radar. That led to their conclusion that "...the lower density assumption…yielded

https://doi.org/10.5194/amt-2022-317
Preprint. Discussion started: 23 January 2023

Atmospheric Measurement Techniques Discussions

closer correspondence to observed reflectivities." Their recommendation for S as a function of Z - hereafter the $S(\rho_1)/Z$ relationship - is $S = 0.39 \cdot Z^{0.58}$. In addition to variance in their values of S, coming from a dependence on density, PV11 state that a value of S derived via their $S(\rho_1)/Z$ relationship is uncertain by a factor-of-ten. This uncertainty is evident in the variance seen about the $S(\rho_1)/Z$ relationship in Fig. 11 of PV11. Those investigators, and Geerts et al. (2010), attributed the variance to use of two-dimensional snow particle imagery in calculations of S and to actual variations of density and shape not accounted for in the calculations. Error associated with the radar-retrieved reflectivities reported in PV11 contributed only marginally to the factor-of-ten uncertainty.

Our focus is the W-band S/Z relationship for rimed snow particles. Section 2 describes the setting of our study, the instruments we deployed, and recordings we obtained using two data acquisition systems. One of the data systems was operated at a ground site and the other on an aircraft. Section 3 is an analysis of the recordings; this section also considers recordings from two additional, but ancillary, ground sites. Our findings are discussed in Sect. 4 and summarized in Sect. 5. An Appendix (Sect. 6) explains how we averaged recordings of near-surface W-band reflectivities and surface-based recordings of snowfall.

https://doi.org/10.5194/amt-2022-317
Preprint. Discussion started: 23 January 2023

Atmospheric Measurement Techniques Discussions Open Access EGU

2 - Site, Aircraft, and Instruments

2.1 - Site

We analyzed aircraft and ground data from 14/15 December 2016, when the analyzed snowfall event spanned a UTC date change, and from 3 January 2017. The ground data were acquired in a forest/prairie ecotone on the eastern slope of the Medicine Bow Mountains in southeastern Wyoming (Figs. 1a-b). No ground-based observers were deployed during the two snowfall events we analyzed.

At one of three ground sites (HP in Figs. 1a-b) we deployed a hotplate precipitation gauge (Rasmussen et al. 2011; Zelasko et al. 2018), a GPS receiver, and a data acquisition system. Once per second, the data system ingested a hotplate-generated data string, combined that with time-of-day from the GPS receiver (Coordinated Universal Time (UTC)), and recorded the merged hotplate/UTC data string. The absolute accuracy of the GPS time stamp is no worse than 2 s.

Overflights of the hotplate were done by the University of Wyoming King Air (WKA) on 14/15 December 2016 and on 3 January 2017. Data acquisition on the WKA was also synchronized with UTC, but with much better accuracy than at the hotplate. Measurements of wind (speed and direction), temperature, and relative humidity from the US-GLE AmeriFlux tower (AF in Figs. 1a-b) are also components of our analysis. The AmeriFlux data were provided to us as 30-minute averages (AmeriFlux 2021; Marlow et al. 2022).

https://doi.org/10.5194/amt-2022-317
Preprint. Discussion started: 23 January 2023

Atmospheric Measurement Techniques
Discussions

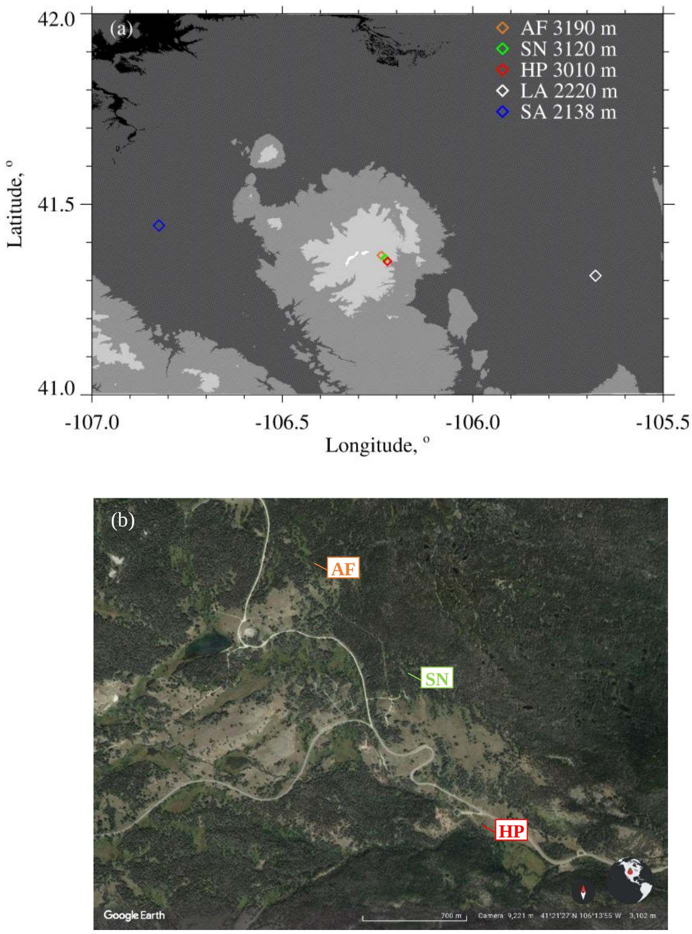

Figure 1 – (a) Southeast Wyoming, airports near the communities of Saratoga, WY (SA) and Laramie, WY (LA), and the ground sites: AF = US-GLE AmeriFlux tower, SN = Brooklyn Lake SNOTEL, and HP = hotplate. Altitudes of the airports and ground sites are in the legend. Altitude thresholds for the digital elevation map are 1500, 2000, 2500, 3000, and 3500 meters. (b) Close up of the AF, SN, and HP ground sites (from © Google Earth).

https://doi.org/10.5194/amt-2022-317
Preprint. Discussion started: 23 January 2023

Atmospheric Measurement Techniques Discussions

2.2 - University of Wyoming King Air (WKA)

We analyzed the following WKA measurements: aircraft position, ambient temperature, snow particle imagery, and three moments of the cloud droplet size distribution function. A Cloud Droplet Probe (CDP; Faber et al. 2018) was the basis for the droplet size distribution measurements and the derived moments. The latter are droplet concentration (N), cloud liquid water content (LWC), and mean droplet diameter (<D>). Snow particle imagery was obtained using a precipitation particle imaging probe (2DP; Korolev et al. 2011) and a cloud particle imaging probe (2DS; Lawson et al. 2006). These acquired two-dimensional images of particles between 200 to 6400 μm (2DP) and between 10 to 1280 μm (2DS).

2.3 - Wyoming Cloud Radar (WCR)

Measurements from the Wyoming Cloud Radar (WCR), operated on the WKA, were also analyzed. We analyzed values of the vertical-component snow particle Doppler velocity retrieved from below the WKA using the WCR's down-looking antenna. Our starting point for that analysis is the Level 2 WCR data which has snow particle Doppler velocities corrected for aircraft motion (Haimov and Rodi 2013). We use V_D to symbolize the corrected vertical-component Doppler velocity and adopt the convention that $V_D > 0$ indicates upward snow particle motion. Level 2 values of Z retrieved using the up-looking and down-looking WCR antennas were also analyzed.

The Level 2 WCR sampling was different on the two flight days and this difference is indicated in Table 1. The flights were conducted in preparation for the SNOWIE field project (Tessendorf et al. 2019) and were flown from the Laramie, WY Airport ("LA" in Fig. 1a).

https://doi.org/10.5194/amt-2022-317
Preprint. Discussion started: 23 January 2023

Atmospheric Measurement Techniques Discussions

174 Table 1 – Level 2 WCR sampling and the WKA overflight time

Date	Level 2 WCR Vertical Sampling, m	Level 2 WCR Along-track Sampling, s	Overflight Time, UTC
14/15 December 2016	23	0.23	00:00:38 (15 December 2016)
3 January 2017	30	0.36	20:32:03

https://doi.org/10.5194/amt-2022-317
Preprint. Discussion started: 23 January 2023

Atmospheric Measurement Techniques Discussions

2.4 - Hotplate Gauge

Algorithms used to process hotplate measurements are described in Rasmussen et al. (2011), Boudala et al. (2014), and Zelasko et al. (2018). Henceforth, these are referred to as R11, B14, and Z18, respectively. In this section, we describe how we analyzed hotplate measurements acquired at the HP site.

Four measurements fundamental to the steady state energy budget of the hotplate's temperature-controlled up-viewing plate are output by the hotplate microprocessor as one-minute running averages (Z18). These running averages were merged with the GPS time and recorded at 1 Hz by the data acquisition system (Sect. 2.1). The four measurements are electrical power supplied to the plate, ambient temperature, wind speed, and solar irradiance. With these measurements, calibration data (Marlow et al. 2022), and the algorithm described in Z18, we calculated the liquid-equivalent snowfall rate. The latter is not corrected for the snow particle undercatch.

Marlow et al. (2022; their Figure 4b) report the relationship between snow particle catch efficiency and wind speed that we applied in calculations of the undercatch-corrected liquid-equivalent snowfall rate (S, mm h^{-1}). There are three bases for this relationship. The first is the catch efficiencies R11 derived from measurements they obtained using a weighing gauge operated within a double fence intercomparison reference shield and a hotplate gauge. R11 plotted their hotplate catch efficiencies versus wind speeds measured at 10 m AGL (their Figure 8). The second is Marlow et al.'s adjustment of R11's 10 m AGL wind speeds to 2 m AGL. The basis for that adjustment is surface boundary layer parameters derived for R11's site (Kochendorfer et al. 2018) and Panofsky and Dutton (1984; their Eq. 6.7). The adjustment was made because the hotplate-reported wind speeds, both here and in Marlow et al. (2022), were

https://doi.org/10.5194/amt-2022-317
Preprint. Discussion started: 23 January 2023

acquired at approximately 2 m above the snowpack surface. The third is a validation of the Marlow et al. (2022) undercatch relationship. That was done by comparing values of S from the hotplate gauge and a SNOTEL pillow gauge (Serreze et al. 1999). In that validation (Marlow et al. 2022; their Figure 10a), the SNOTEL pillow gauge was at the SN site and the hotplate was at the HP site. The SN and HP sites are in Figs. 1a-b.

We also analyzed values of wind speed output by the hotplate microprocessor (U_{PRO}). The basis for this hotplate-derived wind speed is a steady state energy budget of the hotplate's temperature-controlled down-viewing plate and a proprietary algorithm (R11 and Z18). The U_{PRO} were reported by the hotplate as one-minute running averages and we recorded these at 1 Hz. Examples are the gray dots in Fig. 2. Additionally, we calculated and analyzed one-minute-averaged values of U_{PRO} and the corresponding standard deviations. Examples of these are the black circles and the short vertical line segments, respectively, in Fig. 2.

https://doi.org/10.5194/amt-2022-317
Preprint. Discussion started: 23 January 2023

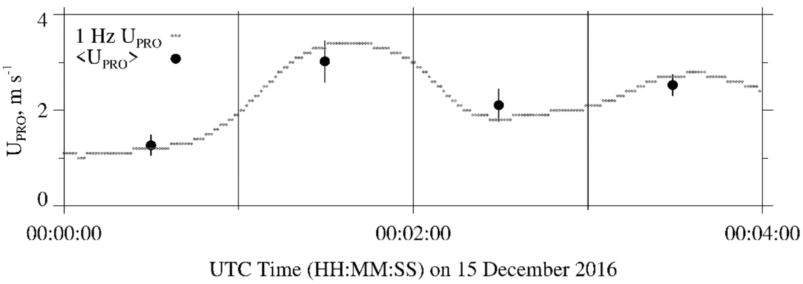

Figure 2 – Hotplate wind speed measurements (U_{PRO}) 00:00:00 to 00:04:00 on 15 December 2016. Gray dots are the one-minute running-average U_{PRO} recorded at 1 Hz. Black circles are the one-minute-averaged U_{PRO} (± 1 standard deviation).

https://doi.org/10.5194/amt-2022-317
Preprint. Discussion started: 23 January 2023

Atmospheric Measurement Techniques Discussions

3 - Analysis

3.1 - WKA Overflight Time

The focus of our analysis is the two WKA flight segments shown in Figs. 3a-b. The maps shown in the figures have the three ground sites (AF, SN, and HP) and the WKA flight tracks (white line). The beginning-to-end time interval for the flight tracks is 100 s and these are divided into ten 10-second intervals. The 10 s intervals are indicated with white diamonds. With the exception of the turn evident in Fig. 3b, the flight tracks are straight and level and the track direction is approximately upwind to downwind.

Times that the WKA was closest to the HP site were evaluated by finding the point on the flight track where the horizontal position of the WKA was closest to the hotplate's coordinates. These times are symbolized t_O and are referred to as overflight times. In Figs. 3a-b the downwind end of the flight tracks end at the overflight time. The latitude/longitude position of the aircraft was within 390 m of the hotplate at the overflight times. Table 1 has the overflight times on the two flight days.

3.2 - Correction of Doppler Velocity

We accounted for bias in V_D (Sect. 2.3) due to deviation of the down-looking WCR antenna from vertical. This was done by applying the correction described in Zaremba et al. (2022) (their Eq. A4). The west-to-east and south-to-north particle velocities used in the correction were assumed equal to component wind velocities. The latter were expressed as linear functions of altitude using the information in the penultimate and last columns of Table 2. The component velocities as functions of altitude and the linear equations relating velocity and altitude are provided in the Appendix.

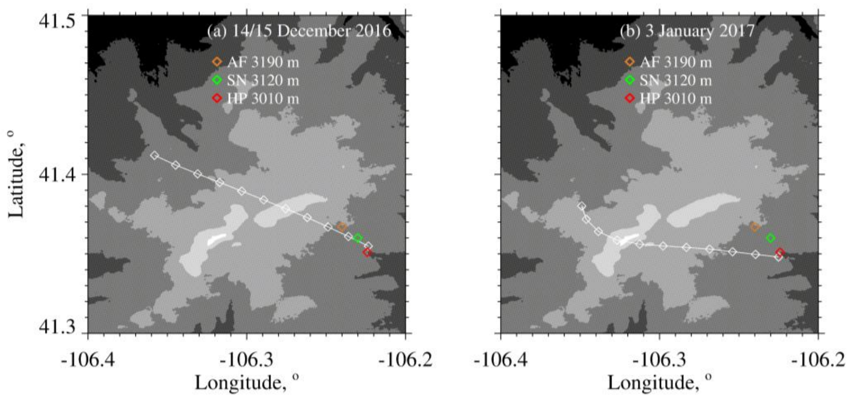

Figure 3 – (a) WKA flight track on 14/15 December 2016 for time interval = overflight time - 100 s to the overflight time. (b) WKA flight track on 3 January 2017 for time interval = overflight time - 100 s to the overflight time. The white diamonds on the tracks are separated, in time, by 10 s. Altitude thresholds for the digital elevation maps are 2600, 2800, 3000, 3200, 3400, and 3600 meters. Altitudes of the ground sites are in the legend.

https://doi.org/10.5194/amt-2022-317
Preprint. Discussion started: 23 January 2023

Atmospheric Measurement Techniques
Discussions

Table 2 – Aircraft and atmospheric state averages

Date	WKA [a] Track Altitude, m	WKA [a] T, °C	AF [b] T, °C	AF [b] RH, %	WKA [a, c] Track Vector	WKA [a, c] Wind Vector	AF [b, c] Wind Vector
14/15 December 2016	4546	-13.9	-6.3	86	310 / 130	274 / 32	250 / 8.5
3 January 2017	4196	-21.7	-14.6	77	280 / 120	265 / 27	260 / 5.4

[a] Altitude, temperature, track vector, and horizontal wind vector data obtained by averaging 1 Hz WKA measurements. The averaging interval is 60 s and the interval starts at the overflight time, minus 60 s, and ends at the overflight time.

[b] Temperature, relative humidity, and horizontal wind vector data from sensors on the US-GLE AmeriFlux tower (Sect. 2.1). The wind sensor was deployed at 26 m AGL (3223 m MSL) and the T/RH sensor was deployed at 23 m AGL (3220 m MSL). The AF measurements correspond to 30-minute averages closest to the overpass time. In the AF data set time stamps on the relevant AF recordings are 00:00 UTC (15 December 2016) and 20:30 UTC (3 January 2017).

[c] Vectors are presented in the following format: Direction of motion (degree relative to true north) / speed (m s^{-1}).

https://doi.org/10.5194/amt-2022-317
Preprint. Discussion started: 23 January 2023

3.3 - Hotplate Measurement of Wind Speed

Here we compare the hotplate-derived wind speed - symbolized U_{PRO} (Z18) - to wind speed derived using an R.M.Young rotating anemometer (R.M.Young 2001). The second of these two speeds we symbolize U_{RMY} and we note that the basis for the first (U_{PRO}) is a proprietary algorithm (Sect. 2.4). We are doing this comparison because B14 showed that U_{PRO} can be high-biased, relative to a conventional anemometer, and because U_{PRO} is the primary determinant of the rate that the up-viewing plate dissipates sensible heat energy. Diagnosis of that heat transfer rate is our basis for calculating the liquid-equivalent snowfall rate (Z18). The U_{PRO} also determines the snow particle catch efficiency. The latter is our basis for calculating the undercatch-corrected liquid-equivalent snowfall rate (Sect. 2.4).

Three years before the wind speed comparison presented here, we attempted to compare the U_{PRO} reported by our hotplate[2] and wind speed reported by a WXT520 Vaisala weather transmitter equipped with an ultrasonic anemometer (Vaisala 2012). These instruments were operated at the HP site in Fig. 1b. However, that data set was difficult to interpret because we did not correctly record the desired 1 Hz wind speed measurements from the WXT520. The comparison reported here was done at the Laramie, WY Airport in December 2019 and January 2020. Compared to the HP site, the Laramie Airport site (indicated LA in Fig. 1) is free of obstruction, out to 120 m, and experiences larger wind speeds. By mounting the hotplate and the R.M.Young anemometer on rigid metal pipes, the hotplate's heated horizontal surfaces (the up- and down-viewing plates seen in Figure 1 of Z18) and the anemometer's spinning axis (oriented horizontally) were both positioned at 2 m AGL. The pipes were separated horizontally by 5 m.

[2] The hotplate used here is the device described in Wolfe and Snider (2012), in Z18, and in Marlow et al. (2022).

https://doi.org/10.5194/amt-2022-317
Preprint. Discussion started: 23 January 2023

Atmospheric Measurement Techniques Discussions

There was no precipitation on the days selected for the wind speed comparisons. The values of U_{PRO} and U_{RMY} we analyzed were recorded with a data system that time stamped the 1 Hz U_{PRO} and 1 Hz U_{RMY} with a relative timing accuracy no worse than 1 s.

A wind speed comparison - from 13 December 2019 - is shown in Fig. 4a. U_{PRO} was brought into the comparison by sampling it once per minute from files containing 1 Hz recordings of the one-minute running-average U_{PRO} (Sect. 2.4). U_{RMY} was brought into the comparison by starting with files containing 1 Hz recordings and converting these to one-minute averages. Fig. 4a shows no evidence of bias and Fig. 4b demonstrates that the average absolute departure between the U_{PRO} and U_{RMY} (both one-minute averages) is no larger than 0.5 m s^{-1}. Table 3 has eight more precipitation-free comparisons. Included in the table are temperature and wind speed averaged over the comparison intervals (4 to 20 UTC), the slope of the linear-least-squares fit line (forced through the origin), and the lower and upper quartiles of the slope. We calculated the quartiles using the method of Wolfe and Snider (2012). In contrast to Figs. 4a-b, Figs. 4c-d make the comparison using 1 Hz values of U_{PRO} and U_{RMY}. The larger scatter and larger average absolute departure seen in these panels is a consequence of the hotplate's limited time response, compared to the R.M.Young. We quantify the hotplate's response time in terms of a thermal response time. During wintertime at the Laramie Airport, and with wind speed at 5 m s^{-1}, the down-viewing plate's thermal response time is 60 s (results not shown). Because the temperature of down-viewing plate is actively controlled, this does not translate to a 60 s lag between changes in wind speed and the hotplate response. The U_{PRO}/U_{RMY} departure is most evident at $U_{PRO} > 5$ m s^{-1} (Fig. 4d) but this is not a concern for U_{PRO} on 14/15 December 2016 or on 3 January 2017. As we show below, the U_{PRO} was less than 5 m s^{-1} at the hotplate during the two WKA overflights.

https://doi.org/10.5194/amt-2022-317
Preprint. Discussion started: 23 January 2023

Atmospheric Measurement Techniques Discussions
Open Access

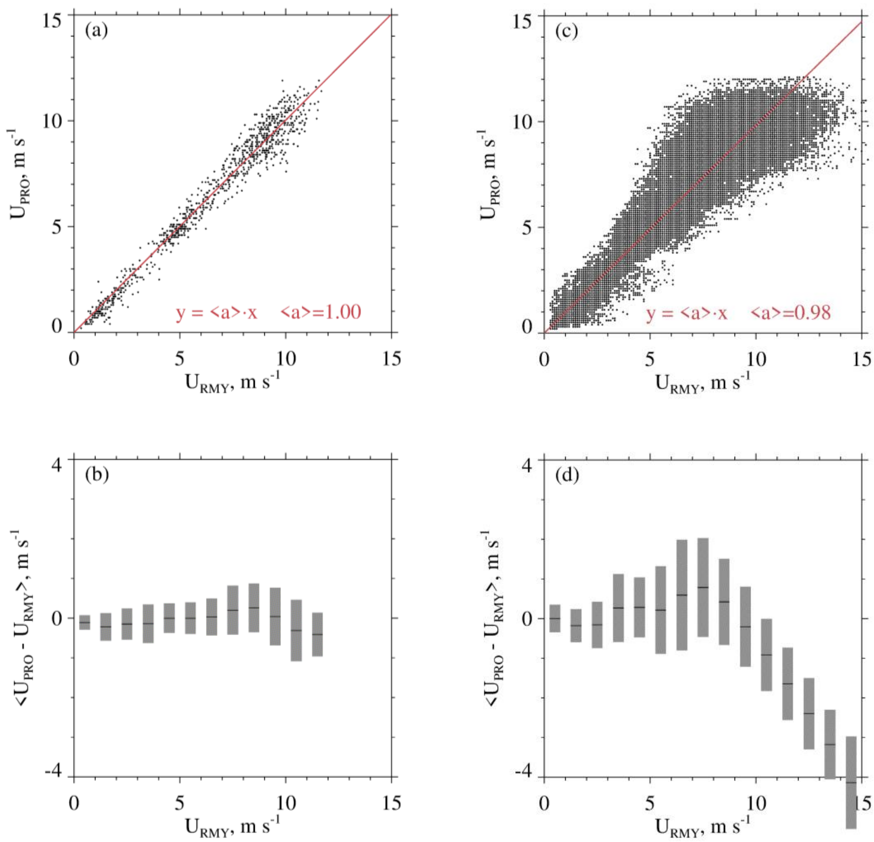

Figure 4 – (a) Scatterplot of one-minute-averaged U_{PRO} and one-minute-averaged U_{RMY}. Measurements were acquired at the Laramie, WY Airport 13 December 2019. The red line is a linear-least-squares fit line (forced through the origin). (b) Average departure between one-minute-averaged U_{PRO} and one-minute-averaged U_{RMY}. Average departures are computed for discrete U_{RMY} intervals and the averages are indicated with short black horizontal lines. Gray bars indicate ± 1 standard deviation. (c) Same as in (a) except 1 Hz values of U_{PRO} and U_{RMY}. (d) Same as in (b) except for 1 Hz values of U_{PRO} and U_{RMY}.

https://doi.org/10.5194/amt-2022-317
Preprint. Discussion started: 23 January 2023

Atmospheric Measurement Techniques Discussions

Table 3 - U_{PRO} versus U_{RMY} correlations

Date, UTC [1]	<T> [2], °C	<U> [2], m s^{-1}	<a> [3]	a [4] First Quartile	a [4] Third Quartile
7 December 2019	-0.40	5.40	1.00	0.90	1.04
8 December 2019	2.70	4.10	0.99	0.90	1.04
10 December 2019	-5.20	3.80	0.99	0.83	1.04
13 December 2019	-1.50	6.60	1.00	0.93	1.06
18 December 2019	-6.20	3.60	0.99	0.92	1.04
19 December 2019	-6.90	2.70	0.95	0.84	0.99
6 January 2020	-6.40	8.80	1.01	0.96	1.06
8 January 2020	0.30	4.20	1.00	0.87	1.05
11 January 2020	-7.20	7.00	1.02	0.97	1.08

[1] Statistics presented are based on one-minute-averaged U_{PRO} and one-minute-averaged U_{RMY} measurements made between 04:00 to 20:00 UTC.

[2] Averaged temperature and interval-averaged wind speed

[3] Slope of the one-minute-averaged U_{PRO} versus one-minute-averaged U_{RMY} linear-least-squares fit line, forced through the origin

[4] Quartiles of the slope (see text)

https://doi.org/10.5194/amt-2022-317
Preprint. Discussion started: 23 January 2023

Atmospheric Measurement Techniques Discussions

3.4 - WCR Measurements

Figure 5 has WCR and WKA measurements starting 100 s prior to t_O and completing at t_O. The sequences in Figs. 5a and 5c are reflectivities from both the up- and down-looking antennas. In Fig. 5a the flight track (black dashed horizontal line) is at 4550 m and in Fig. 5c the flight track is at 4200 m. At the t_O in Fig. 5a, below the WKA, the maximum radar echo is +6 dBZ (Z = 4 mm^6 m^{-3}) while in Fig. 5c that maximum is -3 dBZ (Z = 0.5 mm^6 m^{-3}). Supercooled liquid water was detected as the aircraft approached the ridgeline (Fig. 5b) and during the last 3 seconds of the time sequence in Fig. 5d. During these encounters with supercooled liquid, the maximum LWC values were 0.03x10^{-3} and 0.08x10^{-3} kg m^{-3} on 14 December 2016 and 3 January 2017, respectively. Values of N (Sect. 2.2) at times of maximal LWC were 3x10^6 and 100x10^6 m^{-3} on 14 December 2016 and 3 January 2017, respectively. Even on 3 January 2017, the <D> (Sect. 2.2) associated with maximum LWC was sufficient for hexagonal plate crystals with diameter larger than 100 μm to collide with the observed droplets with efficiencies > 0.1 (Wang and Ji 2000).

We spatially averaged the values of Z we compared with time-averaged values of S. There are two reasons for this: 1) As discussed in Sect. 3.1, the WCR did not sample Z exactly over the hotplate, and furthermore, the width of radar beam at 1500 m range - roughly the distance between the aircraft and the ground at the overflight times - is 30 m and thus considerably smaller than the minimum horizontal distance between the aircraft and the HP. 2) Compared to the WCR, the hotplate is a relatively slow-response measurement system whose output is commonly averaged over one-minute intervals (Z18).

https://doi.org/10.5194/amt-2022-317
Preprint. Discussion started: 23 January 2023

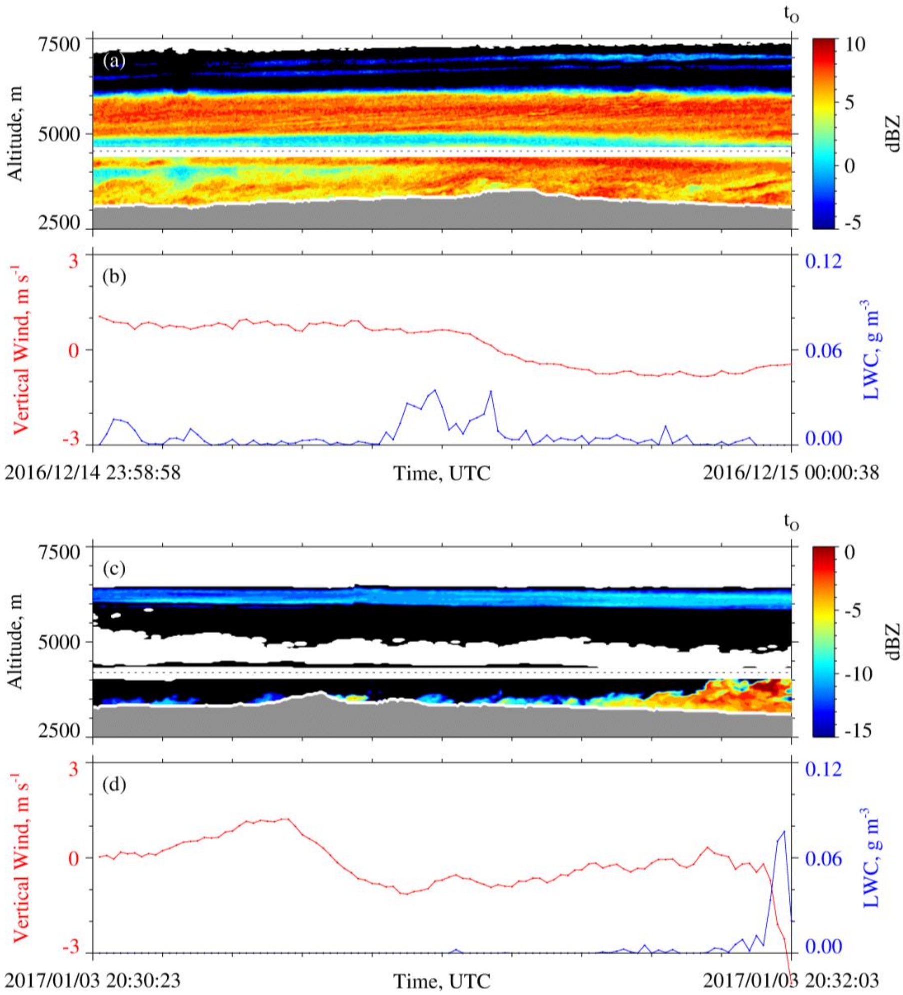

Figure 5 – (a) 100 s of WCR reflectivity from 14/15 December 2016 ending at t_O. (b) 100 s of LWC and gust probe vertical wind velocity from 14/15 December 2016 ending at t_O. (c) 100 s of WCR reflectivity from 3 January 2017 ending at t_O. (d) 100 s of LWC and gust probe vertical wind velocity from 3 January 2017 ending at t_O. In (a) and (c), above and below the flight track is the roughly 200-m-deep WCR blind zone, reflectivity above (below) the flight track is from the up-looking (down-looking) WCR antenna, black indicates reflectivity [dBZ] smaller than minimum indicated in the color bar, white immediately above the terrain indicates echo that was discarded because of ground clutter, and white above the ground clutter and outside of the blind zone indicate dBZ < minimum detectable signal.

https://doi.org/10.5194/amt-2022-317
Preprint. Discussion started: 23 January 2023

Our averaging scheme starts with the HP averaging intervals begun at t_O and at t_O + 60 s. The duration of these intervals is one minute. Figure 6a is a schematic of an HP averaging interval started at t_O , Fig. 6b is a schematic of the corresponding WCR averaging domain, and Figs. 6c-d are schematics of an adjacent averaging interval/domain. Figures 6a and 6c also show that the indexes $i=0$ and $i=1$ are used to indicate HP averaging intervals begun at t_O and t_O + 60 s, respectively. Figures 7b and 8b show hotplate snowfall measurements from 14/15 December 2016 and 3 January 2017 and how we label the HP averaging intervals begun at t_O . In these and subsequent figures, colored circles surround the indexes, blue is used to color-code 15 December 2016, and red is used to color-code 3 January 2017. The Appendix explains the averaging in greater detail. Two aspects not discussed here, but are discussed in the Appendix, are how the “i” indexes were used to calculate the WCR averaging start and end times and how the lines defining the top of the WCR averaging domains, seen in Fig. 6b and 6d, were calculated.

Figure 9a and Fig. 10a have enlarged views of the reflectivity structures recorded on the two flight days. Different from Fig. 5a and Fig. 5c, these measurements are only from the WCR’s down-looking antenna. Additional differences are the following: 1) The plots are set up so that Z and V_D structures downwind of the hotplate can be seen. These structures are discussed in the following section. 2) The WCR measurements are shown for 50 s of flight. With the WKA ground speed approximately 125 m s^{-1} (Table 2), the distance along the abscissa is 6250 m. 3) Colored circles that surround the $i=0$ index are placed below the WCR averaging domains (reflectivity and Doppler velocity). The domains are drawn with solid black lines and these are

https://doi.org/10.5194/amt-2022-317
Preprint. Discussion started: 23 January 2023

Atmospheric Measurement Techniques Discussions

seen to overlay both the Z data (Fig. 9a and Fig. 10a) and the V_D data (Fig. 9b and Fig. 10b). Consistent with Fig. 6b, and the Appendix, one of these black lines is vertical and the other is negatively sloped.

https://doi.org/10.5194/amt-2022-317
Preprint. Discussion started: 23 January 2023

Atmospheric Measurement Techniques
Discussions

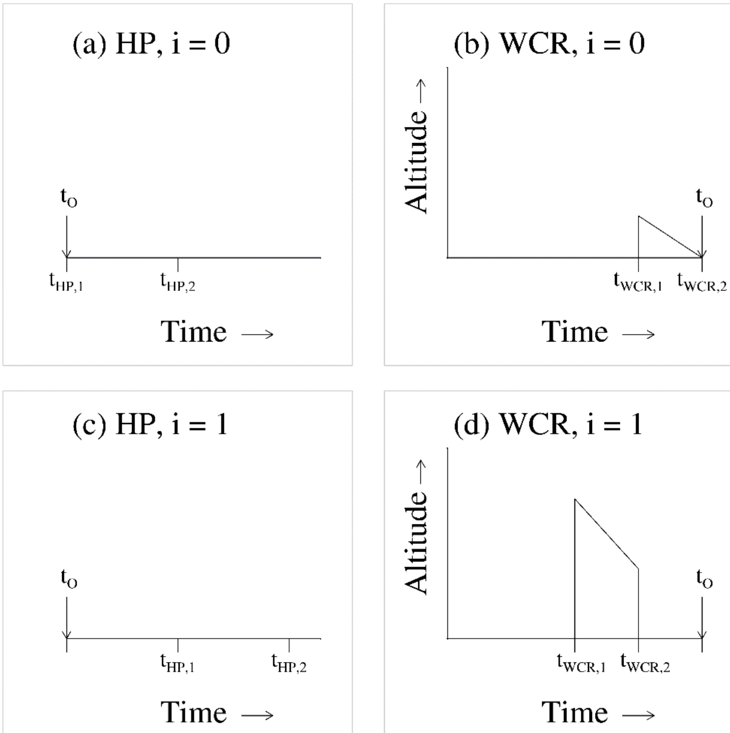

Figure 6 – (a and c) Schematic diagrams of the $i = 0$ and $i = 1$ one-minute HP averaging intervals. (b and d) Schematic diagrams of the $i = 0$ and $i = 1$ WCR averaging domains with the lowest-retrievable weather target at the low end of the ordinate. The t_O is shown in all panels.

https://doi.org/10.5194/amt-2022-317
Preprint. Discussion started: 23 January 2023

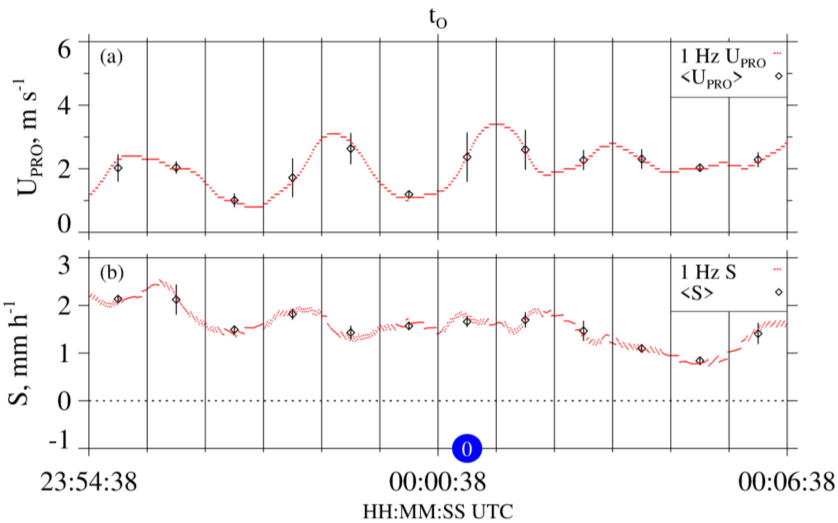

Figure 7 – Twelve minutes of hotplate data from 14/15 December 2016. (a) Wind speed. (b) Snowfall rate. In (a), red dots are the one-minute running-average U_{PRO}, recorded at 1 Hz, and in (b), red dots are values of S computed using hotplate output recorded at 1 Hz. In both panels the black diamonds are the one-minute-averaged values (± 1 standard deviation). The t_O is shown above the top panel and the large blue circle indicates the $i = 0$ HP averaging interval.

https://doi.org/10.5194/amt-2022-317
Preprint. Discussion started: 23 January 2023

Atmospheric Measurement Techniques
Discussions

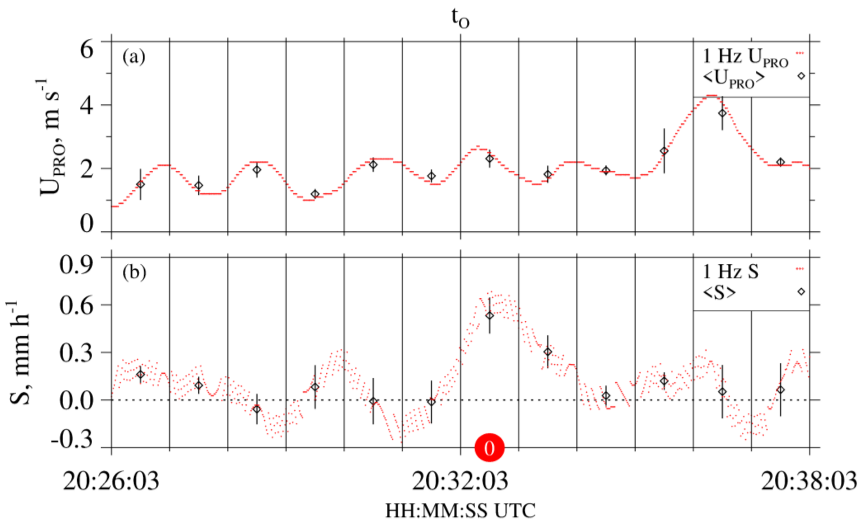

Figure 8 – Twelve minutes of hotplate data from 3 January 2017. (a) Wind speed. (b) Snowfall rate. In (a), red dots are the one-minute running-average U_{PRO}, recorded at 1 Hz, and in (b) red dots are values of S computed using hotplate output recorded at 1 Hz. In both panels the black diamonds are the one-minute-averaged values (± 1 standard deviation). The t_O is shown above the top panel and the large red circle indicates the $i = 0$ HP averaging interval.

https://doi.org/10.5194/amt-2022-317
Preprint. Discussion started: 23 January 2023

Atmospheric Measurement Techniques Discussions

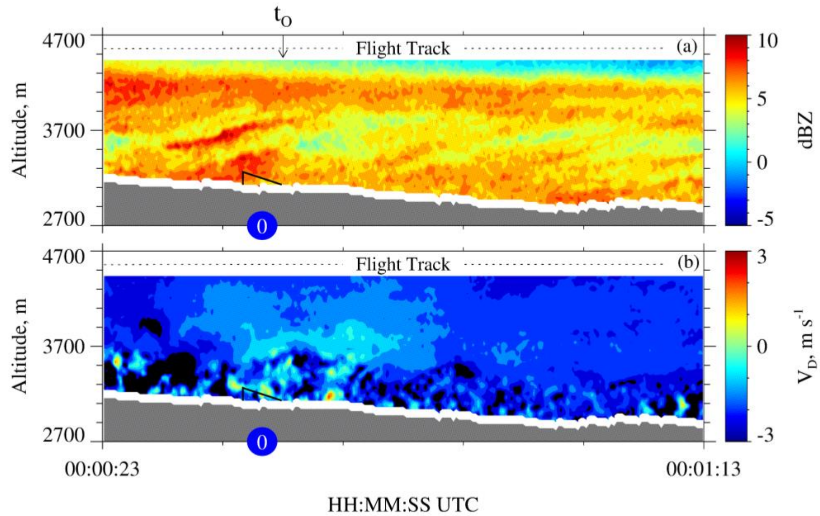

Figure 9 – 50 s of measurements from the down-looking WCR antenna on 15 December 2016. (a) Crossection of reflectivity t_O - 15 s to t_O + 35 s. (b) Crossection of Doppler velocity t_O - 15 s to t_O + 35 s. The t_O is shown above the top panel. In both panels, the solid black lines (vertical and sloped) encompass the $i = 0$ WCR averaging domain and the blue circles have the $i = 0$ index.

https://doi.org/10.5194/amt-2022-317
Preprint. Discussion started: 23 January 2023

Atmospheric Measurement Techniques Discussions

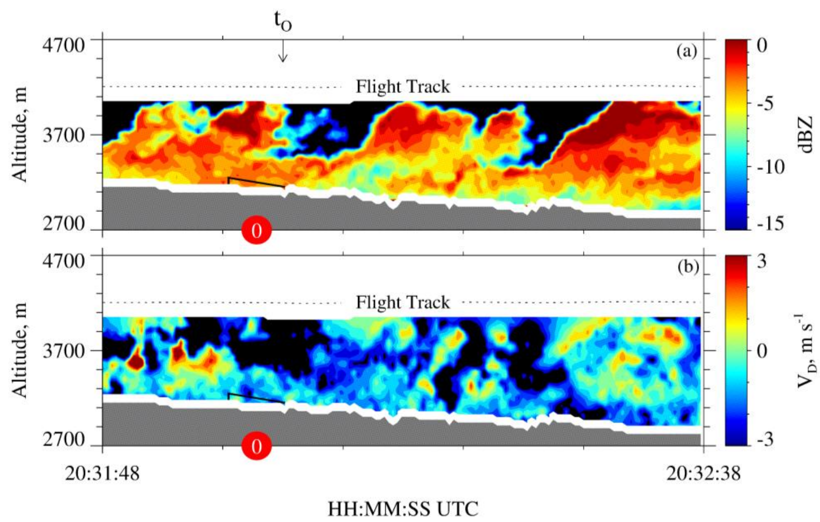

Figure 10 – 50 s of measurements from the down-looking WCR antenna on 3 January 2017. (a) Crossection of reflectivity t_O - 15 s to t_O + 35 s. (b) Crossection of Doppler velocity t_O - 15 s to t_O + 35 s. The t_O is shown above the top panel. In both panels, the solid black lines (vertical and sloped) encompass the $i=0$ WCR averaging domain and the red circles have the $i=0$ index.

https://doi.org/10.5194/amt-2022-317
Preprint. Discussion started: 23 January 2023

Atmospheric Measurement Techniques Discussions

The $i = 0$ averages of S and Z are presented in Table 4 and the corresponding averaging intervals/domains are viewable in Fig. 7b and Fig. 9a (15 December 2016) and in Fig. 8b and Fig. 10a (3 January 2017). The $i = 1$ averages are also presented in Table 4. According to the averaging scheme (Fig. 6), the $i = 1$ HP averaging interval is time-shifted positively compared to the $i = 0$ HP averaging interval and the $i = 1$ WCR averaging domain is time-shifted negatively compared of the $i = 0$ WCR averaging domain. This arrangement of the averaging intervals/domains is one way to average while also accounting for wind advection of the snow particles.

https://doi.org/10.5194/amt-2022-317
Preprint. Discussion started: 23 January 2023

Atmospheric Measurement Techniques
Discussions

Table 4 – Averaged wind, hotplate, and WCR measurements

Date	v_w [a], m s^{-1}	i index	$\langle S \rangle \pm \sigma_S$ [b], mm h^{-1}	WCR Samples [c]	$\langle V_D \rangle$ [d], m s^{-1}	σ_{V_D} [e], m s^{-1}	v_p [f], m s^{-1}	$\langle Z \rangle \pm \sigma_Z$ [g], mm^6 m^{-3}
15 December 2016	7.4	0	1.7±0.1	42	-1.3	0.9	2.2	4.9±2.1
15 December 2016	7.4	1	1.7±0.2	149	-1.8	1.2	3.0	5.6±1.1
3 January 2017	8.9	0	0.5±0.1	20	-0.8	0.8	1.6	0.49±0.05
3 January 2017	8.9	1	0.3±0.1	35	-0.8	0.4	1.2	0.50±0.10

[a] Horizontal wind advection speed (Eq. A5) calculated using values from the penultimate and last columns of Table 2.

[b] One-minute average of the undercatch-corrected liquid-equivalent snowfall rate (± 1 standard deviation). Example averaging intervals are the i = 0 intervals in Fig. 7b and Fig. 8b.

[c] Number of samples used to calculate WCR statistics in the penultimate four columns. The averaging domains (e.g., the i = 0 domains in Figs. 9a-b and 10a-b) encompass the averaged WCR samples.

[d] Average of Doppler velocity within the averaging domains.

[e] Standard deviation of Doppler velocity within the averaging domains.

[f] Maximum likely snow particle speed toward the surface (Eq. A6).

[g] Average reflectivity (± 1 standard deviation)

https://doi.org/10.5194/amt-2022-317
Preprint. Discussion started: 23 January 2023

3.5 - Snow Particle Imagery

In Fig. 9a and Fig. 10a, the time for a snow particle to move the abscissa and ordinate distances is different. The ratio of these two times is 2.6. This follows from our choice of abscissa and ordinate ranges, from values of particle fall speed (1 m s^{-1}) and horizontal wind advection speed (8 m s^{-1}), which we assumed, and from the WKA ground speed (gs ~ 125 m s^{-1}; Table 2). The assumed values are approximately consistent with values of $< V_D >$ and v_w , in Table 4, and with the V_D sign convention (Sect. 2.3). We used $gs = 125$ m s^{-1} to scale (virtually) the time axes in Fig. 9a and Fig. 10a to a horizontal distance. Within the scaled coordinate frames, we assumed that all snow particle trajectories have negative slope ($\Delta z / \Delta x$ = -1 m s^{-1} / 8 m s^{-1} = -0.12) and that all trajectories are stationary. However, both assumptions seem inconsistent with the reflectivity structures in Fig. 5a, where positively-sloped particle fall streaks are evident at ~ 5500 m, inconsistent with Fig. 9a where positively-sloped fall streaks are at ~ 3500 m, and inconsistent with the positively-sloped fall streaks in Fig. 10a. On both flight days, the fall streaks evince particle sources that move horizontally and with a horizontal speed that is larger than the v_w = 8 m s^{-1} we applied in our estimate of the trajectory slope and in our evaluation of the WCR averaging domains (Sect. 3.4). It may be that the source's horizontal speed is comparable to the flight-level WKA-derived horizontal wind (27 to 32 m s^{-1}; Table 2) but we do not have data needed to verify that assertion. Based on our qualitative interpretation of the fall streaks, and the assumption that snow particles followed the fall streaks while both were advecting horizontally, we looked *downwind* of the hotplate - at a time later than t_O in Fig. 9a and Fig. 10a - for particles that became those that produced snowfall at the hotplate.

https://doi.org/10.5194/amt-2022-317
Preprint. Discussion started: 23 January 2023

Atmospheric Measurement Techniques Discussions

Particle images from 15 December 2016 were analyzed using the 2DP. With this instrument the maximum all-in particle size, in the horizontal direction perpendicular to flight, is 6400 μm and the particle size resolution is 200 μm (Sect. 2.2). Within the time interval we picked for this analysis (discussed below), particles sizing in the smaller of the two spectral modes, with mode size ~ 400 μm, were more numerous (results not shown). Because the 400 μm particles are poorly resolved by the 2DP, and the same can be said for somewhat larger particles, those smaller than 1000 μm were excluded from the following analysis. Figure 11a shows imagery from 12 s of measurements acquired near the end of the sequence in Fig. 9a (00:01:02 to 00:01:14). This time interval was selected by tracing backwards from t_O , along the slope of the fall streaks in Fig. 9a, to the flight level. Many of the particles are rounded (indicating riming) and a few have arms likely due to incomplete conversion of branched crystals to rimed snow particles. The mode size corresponding to these images is 1600 μm. No liquid water was detected with these particles (LWC < $0.01\text{x}10^{-3}$ kg m^{-3}; Fuller 2020; her Figure 8), but liquid was detected, at ~ 00:00:00, as the aircraft approached the ridgeline (Sect. 3.4).

Turning to imagery from 3 January 2017, the most appropriate location for analysis would be through the second billow structure evident in Fig. 10a. This billow sourced a fall streak that terminated at the hotplate (i.e., at the time t_O indicated in the figure). However, the aircraft only clipped the top of this billow, and it was only when sampling the billow seen ~ 13 s earlier that larger ice particle concentrations (~ 20,000 m^{-3}) (Fuller 2020; her Figure 10) and larger LWC (> $0.06\text{x}10^{-3}$ kg m^{-3}; Fig. 5d) were detected. Maximum reflectivities were the same in all three billows (Z ~ 1 mm^6 m^{-3}; 0 dBZ), so we assumed that imagery collected in the first billow (20:32:00 to 20:32:02) was representative of what was falling toward the hotplate. The 2DS was used to image these particles (Fig. 11b); with this instrument the maximum all-in

https://doi.org/10.5194/amt-2022-317
Preprint. Discussion started: 23 January 2023

Atmospheric Measurement Techniques Discussions

particle size, in the horizontal direction perpendicular to flight, is 1280 µm and the size resolution is 10 µm (Sect. 2.2). Most of the objects in Fig. 11b appear to be rimed and their mode size is ~ 400 µm. It is also noted that we eliminated particles smaller than 100 µm from these images, however, compared to the ~ 400 µm particles those smaller than 100 µm were significantly less abundant (results not shown).

https://doi.org/10.5194/amt-2022-317
Preprint. Discussion started: 23 January 2023

Atmospheric Measurement Techniques Discussions

(a)

(b)

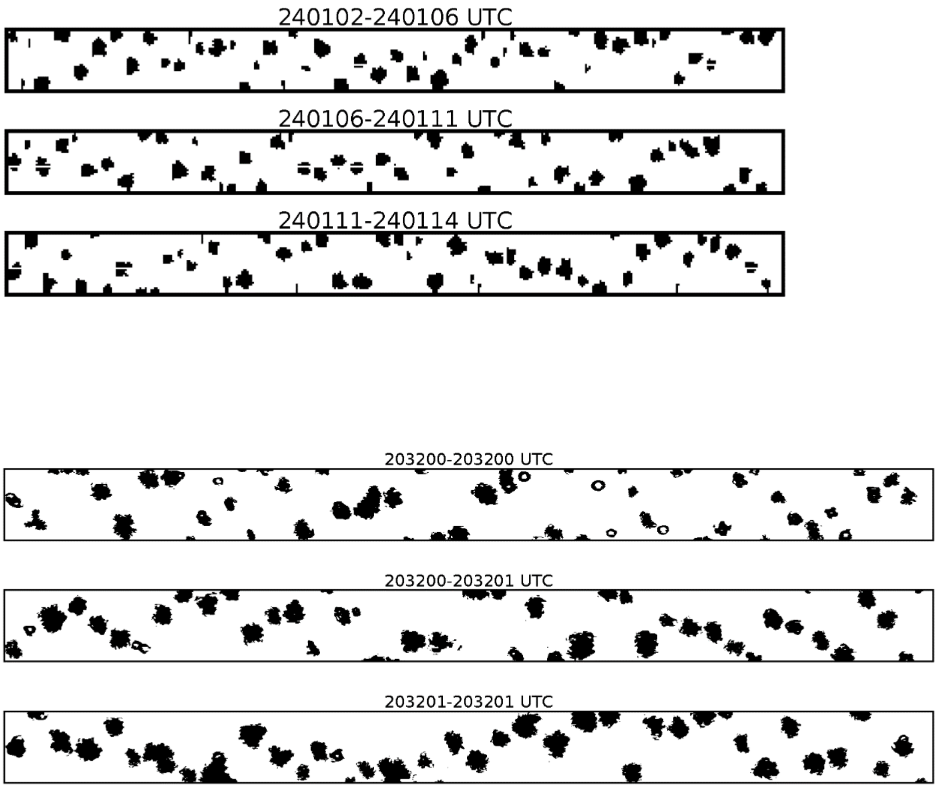

Figure 11 – (a) 2DP particle imagery from 15 December 2016. The height of the strips is 6400 μm. These particles are estimated to be representative of those that fell from flight level toward the hotplate. (b) 2DS particle imagery from 3 January 2017. The height of the strips is 1280 μm. These particles are estimated to be representative of those that fell from flight level toward the hotplate.

https://doi.org/10.5194/amt-2022-317
Preprint. Discussion started: 23 January 2023

Atmospheric Measurement Techniques Discussions

3.6 – S/Z Relationships

The S/Z pairs presented by PV11 in their Figure 11 vary by a factor-of-ten about their best-fit relationship ($S(\rho_1)/Z$). Those results are shown in Fig. 12 with black circles and a black line. Our S/Z pairs are presented in Table 4 and are plotted in Fig. 12 where we used the indexes ($i=0$ and $i=1$) to indicate the averaging intervals/domains. Our data pairs plot above the $S(\rho_1)/Z$ relationship but within the variability.

https://doi.org/10.5194/amt-2022-317
Preprint. Discussion started: 23 January 2023

Atmospheric Measurement Techniques Discussions

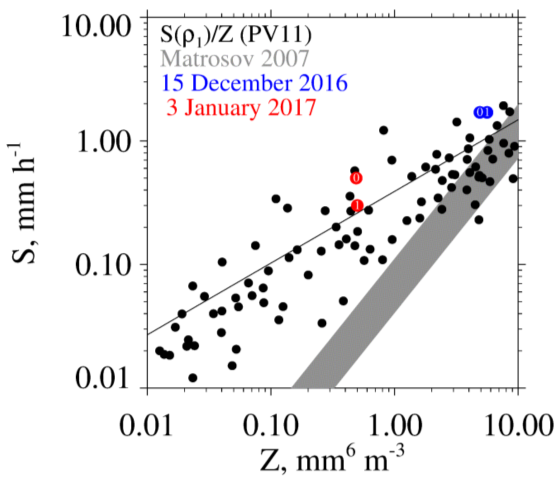

Figure 12 – Snowfall rate (S) versus radar reflectivity (Z). The S(ρ1)/Z data points are from PV11 (their Figure 11). The S(ρ1)/Z relationship and the upper- and lower-limit Matrosov (2007) S/Z relationships are presented as math functions in Sect. 1. Results for $i = 0$ and $i = 1$ averaging intervals/domains are shown with colored circles.

https://doi.org/10.5194/amt-2022-317
Preprint. Discussion started: 23 January 2023

Atmospheric Measurement Techniques Discussions

There are two potential biases in the values of S we tabulate (Table 4) and plot (Fig. 12). First, the two snowfall events had flight-level vertical wind velocities that were positive (upward) upwind of the summit, and vice versa downwind of the summit. Except for the strongest downdraft on 3 January 2017, the magnitude of this variance is ~ 1 m s^{-1} (Figs. 5b and 5d). Assuming 1 m s^{-1} was the downward wind immediately over the hotplate, the snow particles would have approached the gauge faster than their fall speed, and especially so on 3 January 2017. Our basis for stating this is fall speeds for the mode sizes discussed in Sect. 3.6 (1600 and 400 μm) and our assumption that the particles were graupel (Table 5). However, the conjectured downdraft speed is likely an overestimate - because of divergence occurring as the draft approached the surface - and because the sizes in Table 5 likely underestimate what fell to the hotplate. Relevant to the last of these assertions, we used the T/RH/altitude measurements (Table 2) to calculate the vertical distance available for growth via riming, and thus for a fall speed increase, between the flight level and the lifted condensation level. Assuming an adiabatically-stratified supercooled cloud and unit collection efficiency (overestimates growth by riming), and no change of particle crossection (underestimates growth by riming), our calculations indicate that relative increases of size and fall speed were 40 and 20 %, respectively, on 3 January 2017, and that these relative increases were a factor-of-two larger on 15 December 2016.

Table 5 – Estimates of snow particle fall speed

Date	Mode Size, µm	Assumed Particle Type	Fall Speed, m s^{-1}	Reference
15 December 2015	1600	graupel	1.4	PV11; assuming ρ_1 in their Figure 5
3 January 2016	400	graupel	0.7	PV11; assuming ρ_1 in their Figure 5

https://doi.org/10.5194/amt-2022-317
Preprint. Discussion started: 23 January 2023

Atmospheric Measurement Techniques Discussions

Second, there is concern that values of S from 3 January 2017 are underestimated. Although, values of S must be > 0, we presented 1 Hz values (red points, Fig. 8b) as small as -0.3 mm h^{-1}. Negative values resulted because we did not impose a threshold of 0 mm h^{-1} on the uncorrected snowfall rates (this thresholding is discussed in Z18) and because negative snowfall rate values (uncorrected for catch inefficiency) are amplified by the gauge-catch correction (Sect. 2.4). The implication is that 0.2 mm h^{-1} could be added to the one-minute averaged values of S in Table 4 and in Fig. 12. Here, the assumption is that an averaged S of -0.2 mm h^{-1}, in Fig. 8b, is indicating no snowfall and no surface deposition of blowing snow; however, because the hotplate was operated autonomously (Sect. 2.1) we have no way to verify the assumption.

https://doi.org/10.5194/amt-2022-317
Preprint. Discussion started: 23 January 2023

Atmospheric Measurement Techniques Discussions

4 – Results

Our paired values of surface-measured precipitation and aircraft-measured radar reflectivity provide evidence - in addition to PV11 - that most prior determinations of the S/Z relationship for W-band radars lead to underestimation of S in situations with rimed snow particles and particularly so in situations with Z smaller than 1 mm^6 m^{-3}. We assert that the underestimate stems from the smaller density implicit in most computationally-based S/Z relationships and especially those which assume that snow particles consist of vapor-grown crystals or aggregates of vapor-grown crystals. Values of density are quite different for these two particle types versus that for rimed snow particles. For example, in Matrosov (2007), assuming a 2 mm aggregate, the density is ~ 30 kg m^{-3}, whereas in PV11, assuming a 2 mm graupel particle, the density is ~ 200 kg m^{-3}.

In the previous paragraph, a cutoff at Z = 1 mm^6 m^{-3} was specified because that is where the separation between the Matrosov (2007) and both our and PV11's WCR observations become evident (Fig. 12). The cutoff was also picked because Kulie et al. (2016) apply it in an analysis of snowfall retrieved using the W-band radar on CloudSat. They concluded that 74% of shallow cumuliform cloud structures, and 37% of nimbostratus cloud structures, have near-surface reflectivities < 1 mm^6 m^{-3}. Depending on which snowfall process dominates in these structures (vapor growth, aggregation, or riming) an alteration of S for Z < 1 mm^6 m^{-3} (e.g., Fig. 12) could have a significant effect on W-band retrievals. For example, the analysis of Kulie et al. 2016 (their Figure 6) suggests that the Greenland, Norwegian, and Barents Seas regions may be susceptible to this alteration.

Some computationally based S/Z relationships (Surussavadee and Staelin (2006) and Kulie and Bennartz (2009)) do plot between PV11's S(ρ_1)/Z relationship - the black line in Fig.

https://doi.org/10.5194/amt-2022-317
Preprint. Discussion started: 23 January 2023

Atmospheric Measurement Techniques Discussions

12 - and Matrosov's upper-limit S/Z relationship (the top of the gray area in Fig. 12). Of these the Surussavadee and Staelin relationship assumes that the snow particles are spheres. This seems reasonable for rimed snow particles but not for the crystal and aggregate types modeled by Matrosov (2007) where the particles are approximated as low-density oblate spheroids with their major axis (on average) oriented horizontal. Because of this, proposed space-based platforms may carry instrumentation that can guide selection of a scene-appropriate S/Z relationship. Both lidar and radiometers can sense supercooled liquid water from space, and if combined with Doppler radar, can diagnose precipitation attributable to rimed snow particles. These approaches are being tested in ground-based field studies (Moisseev et al. 2017; Mason et al. 2018).

https://doi.org/10.5194/amt-2022-317
Preprint. Discussion started: 23 January 2023

Atmospheric Measurement Techniques Discussions

5 - Conclusions

This study is significant because it brings together direct measurements of snowfall rate, measured at the ground, and measurements of reflectivity from an airborne W-band radar. Compared to PV11's $S(\rho_1)/Z$ relationship, shown in Fig. 12, our observations do not depart significantly; however, they do plot somewhat larger. This excess could be consistent with downslope flow that occurs in lee of the Medicine Bow Mountains (Sect. 3.6) or with calculations which indicate that larger density is associated with larger S, in the S-versus-Z coordinate system (PV11), combined with the intrinsic variability of the density of rime ice (Macklin 1962).

If the downslope flow hypothesis is correct, we expect it to manifest as negatively-biased retrievals of S, in settings leeward of a ridgeline, where snowfall is produced by riming, and PV11's $S(\rho_1)/Z$ relationship is applied in the retrieval. This follows because PV11, and all other S/Z relationship developers, do not account for the effect of vertical air motion on S values incorporated into their S/Z relationships. Furthermore, the sign of the hypothesized bias will vary from positive (radar-retrieved S larger than a surface-measured S) to negative (radar-retrieved S smaller than a surface-measured S) in the downwind direction across a ridgeline. Finally, we expect the relative magnitude of the hypothesized biases will be enhanced in a situation where Z is measured, snowfall is produced via the diffusion growth of crystals, and the scene-appropriate S/Z relationship is applied.

https://doi.org/10.5194/amt-2022-317
Preprint. Discussion started: 23 January 2023

Atmospheric Measurement Techniques Discussions

6 - Appendix

This appendix explains how the HP (hotplate) and WCR (Wyoming Cloud Radar) averages were evaluated.

With the overflight time symbolized t_O and i an index equal to either 0 or 1 the start and stop times for a one-minute HP average are

$$t_{HP,1} = t_O + i \cdot 60 \quad \text{(A1)}$$

$$t_{HP,2} = t_O + (i+1) \cdot 60 \quad \text{(A2)}$$

Examples of $t_{HP,1}$ and $t_{HP,2}$ are at the left and right edges of the $i = 0$ one-minute HP averaging intervals in Fig. 7b and Fig. 8b.

The stop time for WCR averaging was calculated as

$$t_{WCR,2} = t_O - i \cdot 60 \cdot v_w / gs \,. \quad \text{(A3)}$$

Here v_w is a wind advection speed (discussed below) and the second term on the rhs is a wind advection distance divided by the WKA (Wyoming King Air) ground speed (gs). The start time for WCR averaging was calculated as

$$t_{WCR,1} = t_{WCR,2} - (1+i) \cdot 60 \cdot v_w / gs \quad \text{(A4)}$$

The wind advection speed (v_w) in Eqs. A3-A4 was calculated using an altitude-dependent west-to-east wind velocity (u) and an altitude-dependent south-to-north wind velocity (v). These altitude-dependent component velocities were calculated using the horizontal wind vectors in the penultimate and last columns of Table 2. Plots of the component velocities versus altitude and the linear functions used to relate component velocities to altitude are presented in Figs. A1a-b.

We assumed an altitude ($z' = 3400$ m) for evaluating the horizontal wind advection vector. This is the altitude of the ridges west and northwest of the HP site (Figs. 3a-b). Picking the altitude to be either $z' = 3200$ m or $z' = 3600$ m does not substantially alter our conclusions.

The WKA track vector (Table 2) defines the vertical plane of the WCR measurements. We assumed that wind advection of snow particles occurred parallel to this vector. With the assumption stated in the previous paragraph, the horizontal wind advection speed (v_w) was calculated as the projection of the horizontal wind vector onto the track vector.

$$v_w = \frac{u(z') \cdot gs_x + v(z') \cdot gs_y}{\left(gs_x{}^2 + gs_y{}^2\right)^{1/2}} . \quad \text{(A5)}$$

In Eq. A5 the west-to-east and south-to-north components of the track vector are symbolized gs_x and gs_y. Vector representations of the track vector are in Table 2. On 14/15 December 2016 and 3 January 2017 the values of v_w are 7.4 and 8.9 m s^{-1}, respectively.

In addition to the properties gs and v_w used to calculate the averaging times (Eqs. A3-A4), the WCR averages were derived using a snow particle downward speed (Eq. A6).

$$v_p = |< V_D >| + \sigma_{V_D} \quad \text{(A6)}$$

Here, v_p is a snow particle downward speed (discussed below), $< V_D >$ is the average of Doppler velocities within an averaging domain, $|< V_D >|$ is the absolute value of the average, and σ_{V_D} is the standard deviation of the average. On both the lhs and rhs of Eq. A6, all properties are greater than zero.

We interpret v_p as the maximum likely snow particle speed toward the surface. There are three reasons for this: 1) For the WCR averaging domains we analyzed, values of $< V_D >$ are

https://doi.org/10.5194/amt-2022-317
Preprint. Discussion started: 23 January 2023

Atmospheric Measurement Techniques
Discussions
Open Access
EGU

consistently less than zero. This indicates that snow particles (on average) were moving toward the surface. 2) Again for the WCR averaging domains we analyzed, σ_{V_D} is comparable to $|<V_D>|$ indicating that turbulent eddies transported snow particles upward and downward at speeds comparable to the fall speed of the snow particles in quiescent air. 3) The V_D are reflectivity weighted (Haimov and Rodi 2013) and are thus indicative of the motion of the largest particles within the WCR viewing volume.

We now focus on the top of the WCR averaging domains shown schematically in Fig. 6. The slope defining this upper boundary was calculated as $-v_p \cdot gs / v_w$. That is, particles below this boundary were moving downward sufficiently fast and horizontally sufficiently slow to advect reasonably close to the hotplate. Starting with diagnosed values of gs and v_w, values of v_p and thus values of the slope, were derived iteratively. The precision of the derived v_p is ± 0.1 m s^{-1}.

https://doi.org/10.5194/amt-2022-317
Preprint. Discussion started: 23 January 2023

Atmospheric Measurement Techniques Discussions

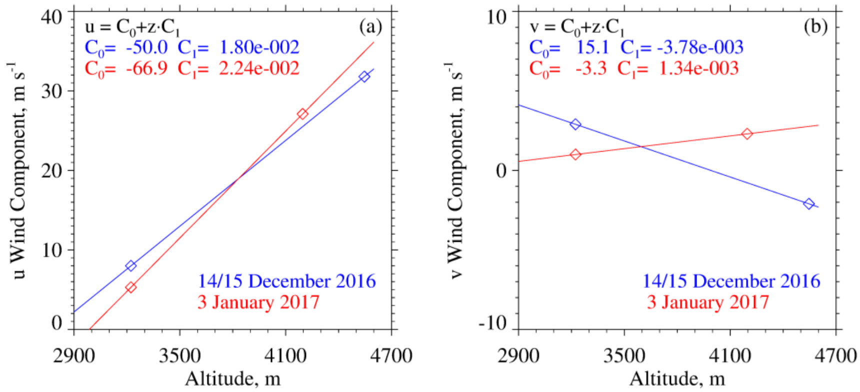

Figure A1 – (a) West-to-east (u) wind velocity derived using measurements from the WKA and the AmeriFlux (AF) tower. Also shown is the altitude-dependent linear function used to relate u to altitude. (b) South-to-north (v) wind velocity derived using measurements from the WKA and AF. Also shown is the altitude-dependent linear function used to relate v to altitude. WKA and AF velocities are presented as vectors in the penultimate and last columns of Table 2.

https://doi.org/10.5194/amt-2022-317
Preprint. Discussion started: 23 January 2023

Atmospheric Measurement Techniques Discussions

Data Availability. The WKA and WCR measurements can be obtained from the SNOWIE data archive of NCAR/EOL, which is sponsored by the National Science Foundation. Hotplate gauge measurements are at https://doi.org/10.15786/20103146. The US-GLE AmeriFlux measurements are at https://ameriflux.lbl.gov/. The Brooklyn Lake SNOTEL gauge measurements are at https://www.wcc.nrcs.usda.gov/snow/.

https://doi.org/10.5194/amt-2022-317
Preprint. Discussion started: 23 January 2023

Author contributions. JRS and MB wrote a successful proposal that funded this research. Field measurements were performed by SF, SM, SH, MB, and JRS. SF wrote her MS dissertation, and this was adapted for this paper by JRS. KS processed the snow particle imagery. AM maintained the measurement sites. All authors contributed to the editing of this paper.

Acknowledgements –

We acknowledge the expert technical assistance provided by David Plummer, Larry Oolman, Zane Little, Brent Glover, Edward Sigel, Thomas Drew, and Brett Wadsworth. We thank SNOWIE project PI Jeffery French, who provided the flight data, Gabor Vali who provided the S/Z data points in Figure 12, and John Frank and John Korfmacher who acquire and maintain the GLE-US AmeriFlux data set. This work was supported by the United States National Science Foundation (Award Number 1850809) and the John P. Ellbogen Foundation.

https://doi.org/10.5194/amt-2022-317
Preprint. Discussion started: 23 January 2023

Atmospheric Measurement Techniques
Discussions

References

AmeriFlux, https://ameriflux.lbl.gov/, 2021

Boudala, F.S., R. Rasmussen, G.A. Isaac, and B. Scott, Performance of Hot Plate for Measuring Solid Precipitation in Complex Terrain during the 2010 Vancouver Winter Olympics, J. Atmos. Oceanic Technol., 31, 437–446, https://doi.org/10.1175/JTECH-D-12-00247.1, 2014

Brock, F. V., and Richardson, S. J., Meteorological Measurement Systems, Oxford University Press, New York, 304 pp., 2001

Cocks, S.B., S.M. Martinaitis, B. Kaney, J. Zhang, and K. Howard, MRMS QPE Performance during the 2013/14 Cool Season, J. Hydrometeor., 17, 791–810, https://doi.org/10.1175/JHM-D-15-0095.1, 2016

Faber, S., French, J. R., and Jackson, R., Laboratory and in-flight evaluation of measurement uncertainties from a commercial Cloud Droplet Probe (CDP), Atmos. Meas. Tech., 11, 3645–3659, https://doi.org/10.5194/amt-11-3645-2018, 2018

Fuller, S.E., Improvement of the Snowfall / Reflectivity Relationship for W-band Radars, MS Thesis, Department of Atmospheric Science, University of Wyoming, 2020

Geerts, B., Q. Miao, Y. Yang, R. Rasmussen, and D. Breed, An Airborne Profiling Radar Study of the Impact of Glaciogenic Cloud Seeding on Snowfall from Winter Orographic Clouds, J. Atmos. Sci., 67, 3286–3302, https://doi.org/10.1175/2010JAS3496.1, 2010

Haimov, S., and Rodi, A., Fixed-Antenna Pointing-Angle Calibration of Airborne Doppler Cloud Radar, Journal of Atmospheric and Oceanic Technology, 30, 2320-2335, https://doi.org/10.1175/JTECH-D-12-00262.1, 2013

Kochendorfer, J., Nitu, R., Wolff, M., Mekis, E., Rasmussen, R., Baker, B., and Jachcik, A, Testing and development of transfer functions for weighing precipitation gauges in WMO-SPICE, Hydrology and Earth System Sciences, 2, 1437-1452, https://doi.org/10.5194/hess-22-1437-2018, 2018

Korolev, A. V., E. F. Emery, J. W. Strapp, S. G. Cober, G. A. Isaac, M. Wasey, and D. Marcotte, Small ice particles in tropospheric clouds: Fact or artifact? Airborne Icing Instrumentation Evaluation Experiment, Bull. Amer. Meteor. Soc., 92, 967–973, https://doi.org/10.1175/2010BAMS3141.1, 2011

Kulie, M. S., and R. Bennartz, Utilizing Spaceborne Radars to Retrieve Dry Snowfall, J. Appl. Meteor. Climatol., 48, 2564–2580, https://doi.org/10.1175/2009JAMC2193.1, 2009

Kulie, M. S., Milani, L., Wood, N. B., Tushaus, S. A., Bennartz, R., and L'Ecuyer, T. S., A Shallow Cumuliform Snowfall Census Using Spaceborne Radar, Journal of Hydrometeorology, 4, 1261-1279, https://doi.org/10.1175/JHM-D-15-0123.1, 2016

https://doi.org/10.5194/amt-2022-317
Preprint. Discussion started: 23 January 2023

Atmospheric Measurement Techniques Discussions

Lawson, R. P., O'Connor, D., Zmarzly, P., Weaver, K., Baker, B., Mo, Q., and Jonsson, H., The 2D-S (Stereo) Probe: Design and Preliminary Tests of a New Airborne, High-Speed, High-Resolution Particle Imaging Probe, J. Atmos. Ocean. Tech., 23, 1462–1477, https://doi.org/10.1175/JTECH1927.1, 2006

Locatelli, J.D. and Hobbs, P.V., Fall speed and masses of solid precipitation particles, J. Geophys. Res., 79, 2185–2197, https://doi.org/10.1029/JC079i015p02185, 1974

Macklin, W.C., The density and structure of ice formed by accretion, Q.J.R.Meteorol.Soc., 88: 30-50. doi:10.1002/qj.49708837504, https://doi.org/10.1002/qj.49708837504, 1962

Marlow, S.A, J.M. Frank, M. Burkhart, B. Borkhuu, S.E. Fuller, and J.R. Snider, Snowfall measurements in mountainous terrain, in revision for the Journal of Applied Meteorology and Climatology, http://www-das.uwyo.edu/~jsnider/JAMC-D-22-0093_6.pdf, 2022

Martinaitis, S.M., S.B. Cocks, Y. Qi, B.T. Kaney, J. Zhang, and K. Howard, Understanding winter precipitation impacts on automated gauge observations within a real-rime system, J. Hydrometeor., 16, 2345-2363, https://doi.org/10.1175/JHM-D-15-0020.1, 2015

Mason, S. L., Chiu, C. J., Hogan, R. J., Moisseev, D., and Kneifel, S., Retrievals of riming and snow density from vertically pointing Doppler radars, Journal of Geophysical Research: Atmospheres, 123, 13,807– 13,834, https://doi.org/10.1029/2018JD028603, 2018

Matrosov, S.Y., Modeling Backscatter Properties of Snowfall at Millimeter Wavelengths, J. Atmos. Sci., 64, 1727-1736, https://doi.org/10.1175/JAS3904.1, 2007

Moisseev, D., von Lerber, A., and Tiira, J., Quantifying the effect of riming on snowfall using ground-based observations, J. Geophys. Res. Atmos., 122, 4019–4037, doi:10.1002/2016JD026272, 2017

Panofsky, H.A. and Dutton, J.A., Atmospheric Turbulence, Wiley-Interscience, New York, 397 pp., 1984

Pokharel, B. and G. Vali, Evaluation of Collocated Measurements of Radar Reflectivity and Particle Sizes in Ice Clouds, J. Appl. Meteor. Climatol., 50, 2104–2119, https://doi.org/10.1175/JAMC-D-10-05010.1, 2011

Rasmussen, R.M., J. Hallett, R. Purcell, S.D. Landolt, and J. Cole, The Hotplate precipitation gauge, J. Atmos. Oceanic Technol., 28, 148-164, https://doi.org/10.1175/2010JTECHA1375.1, 2011

R.M. Young Company, Model 05103 Wind Monitor, 2001

Serreze, M. C., M. P Clark, and R. L. Armstrong, D. A. MacGinnis, and R. S. Pulwarty, Characteristics of the western United States snowpack from snowpack telemetry (SNOTEL) data, Water Resources Research, 35, 2145-2160, https://doi.org/10.1029/1999WR900090, 1999

Skofronick-Jackson, G., and Coauthors, The Global Precipitation Measurement (GPM) Mission for science and society, Bull. Amer. Meteor. Soc., 98, 1679–1695, https://doi.org/10.1175/BAMS-D-15-00306.1, 2017

https://doi.org/10.5194/amt-2022-317
Preprint. Discussion started: 23 January 2023

Atmospheric Measurement Techniques Discussions

Smith, P.L., Equivalent radar reflectivity factors for snow and ice particles, J. Climatol. Appl. Meteor., 23, 1258–1260, https://doi.org/10.1175/1520-0450(1984)023<1258:ERRFFS>2.0.CO;2, 1984

Surussavadee, C. and D.H. Staelin, Comparison of AMSU millimeter-wave satellite observations, MM5/TBSCAT predicted radiances, and electromagnetic models for hydrometeors, IEEE Trans. Geosci. Remote Sens., 44, 2667–2678, 10.1109/TGRS.2006.873275, 2006

Tessendorf, S. A., and Coauthors, A transformational approach to winter orographic weather modification research: The SNOWIE Project, Bulletin of the American Meteorological Society, 100, 71–92, https://doi.org/10.1175/BAMS-D-17-0152.1, 2019

Vaisala, User's Guide, Vaisala Weather Transmitter, WXT520, 2012

Wang, P.K., and W. Ji, Collision Efficiencies of Ice Crystals at Low–Intermediate Reynolds Numbers Colliding with Supercooled Cloud Droplets: A Numerical Study, Journal of the Atmospheric Sciences, 57, 1001-1009, https://doi.org/10.1175/1520-0469(2000)057<1001:CEOICA>2.0.CO;2, 2000

Wilson, J., and E. Brandes, Radar measurement of rainfall—A summary, Bull. Amer. Meteor. Soc., 60, 1048–1058, https://doi.org/10.1175/1520-0477(1979)060<1048:RMORS>2.0.CO;2, 1979

Wolfe, J.P., and J.R. Snider, A relationship between reflectivity and snow rate for a high-altitude S-band radar, J. Appl. Meteor. Climatol., 51, 1111–1128, https://doi.org/10.1175/JAMC-D-11-0112.1, 2012

Zaremba, T.J., and Coauthors, Vertical motions in orographic cloud systems over the Payette River Basin. Part 1: Recovery of vertical motions and their uncertainty from airborne Doppler radial Velocity Measurements, in press at the Journal of Applied Meteorology and Climatology, https://doi.org/10.1175/JAMC-D-21-0228.1, 2022

Zelasko, N., Wettlaufer, A., Borkhuu, B., Burkhart, M., Campbell, L. S., Steenburgh, W. J., and Snider, J.R., Hotplate precipitation gauge calibrations and field measurements, Atmos. Meas. Tech., 11, 441-458, https://doi.org/10.5194/amt-11-441-2018, 2018

Zikmunda, J. and Vali, G., Fall patterns and fall velocities of rimed ice crystals, J. Atmos. Sci., 29, 1334–1347, https://doi.org/10.1175/1520-0469(1972)029<1334:FPAFVO>2.0.CO;2, 1972